*Nano Research* 2018, 11(9): 4735–4743
https://doi.org/10.1007/s12274-018-2058-0
**Research Article**

ISSN 1998-0124
CN 11-5974/O4

# Ultrafast one-step synthesis of N and $Ti^{3+}$ codoped $TiO_2$ nanosheets via energetic material deflagration

Yousong Liu[1], Shuxin Ouyang[2] (✉), Wencan Guo[3], Hehou Zong[1], Xudong Cui[1], Zhong Jin[4] (✉), and Guangcheng Yang[1] (✉)

[1] *Institute of Chemical Materials, China Academy of Engineering Physics, Mianyang 621900, China*
[2] *TU-NIMS Joint Research Center, School of Materials Science and Engineering, Tianjin University, Tianjin 300072, China*
[3] *Institute of Fluid Physics, China Academy of Engineering Physics, Mianyang 621900, China*
[4] *Key Laboratory of Mesoscopic Chemistry of MOE and Collaborative Innovation Center of Chemistry for Life Sciences, School of Chemistry and Chemical Engineering, Nanjing University, Nanjing 210023, China*

**Received:** 9 January 2018
**Revised:** 6 March 2018
**Accepted:** 17 March 2018

**KEYWORDS**

$NaN_3$ deflagration,
N radicals and Na nanoclusters,
ultrafast doping,
N,
$Ti^{3+}$ codoped $TiO_2$,
visible-light response

## ABSTRACT

An energetic-material ($NaN_3$) deflagration method for preparing N- and $Ti^{3+}$-codoped $TiO_2$ nanosheets (NT–$TiO_2$) was developed. In this method, N radicals filled the crystal lattice, and Na clusters captured partial O from $TiO_2$. The deflagration process was fast and facile and can be completed within < 1 s after ignition. The obtained NT–$TiO_2$ exhibited rough surfaces with nanopits and nanoholes. The doping concentration can be regulated by controlling the $NaN_3$ addition. The NT–$TiO_2$ samples showed significant enhancements in the visible-light absorption and photoelectric response. The simultaneously produced N radicals and Na clusters from $NaN_3$ deflagration served as N sources and reduction agents, respectively. Additionally, the high deflagration temperature/pressure improved the reactivity of N radicals and Na clusters. Thus, the present $NaN_3$ deflagration method was demonstrated as an ultrafast and effective approach to fabricate NT–$TiO_2$ with a visible-light response. The proposed $NaN_3$ deflagration method allows the ultrafast synthesis of new functional materials via the efficient deflagration of energetic materials.

## 1 Introduction

Owing to their low cost, low toxicity, high thermal/chemical stabilities, and excellent optical/electronic properties [1], $TiO_2$ materials have attracted extensive attention and been employed for various applications in solar-driven energy conversion [2, 3], paint additives [4], sensors [5], and lithium-ion batteries [6, 7]. In particular, their utilization in solar-energy conversion is limited to the ultraviolet (UV) region owing to the wide bandgap (~ 3.2 eV) of $TiO_2$. Therefore, the extension of the absorption range of $TiO_2$ to the

---

Address correspondence to Guangcheng Yang, ygcheng@caep.cn; Shuxin Ouyang, oysx@tju.edu.cn; Zhong Jin, zhongjin@nju.edu.cn

visible region is strongly desired for energy-conversion applications. Physically, doping impurities into the $TiO_2$ lattice, which generates donor or acceptor states in the bandgap, is an effective method. Dopants, such as metals [8] or nonmetals [9–12], are feasible because of the electronic transition of dopants, which results in additional impurity energy levels in $TiO_2$. Nevertheless, individual doping of a metal or nonmetal cannot remarkably improve the performance of the visible response for $TiO_2$. Codoping of a metal and nonmetal, such as N and Fe or N and $Ti^{3+}$, is a common way to balance the deficiencies of individual doping.

When the synthetic technique is considered, doping of N into $TiO_2$ is cheap and easy. The current N sources, such as $NH_3$ [10, 13–15], $NH_4Cl$ [16, 17], urea [18], and kelp [19], are used to dope N into $TiO_2$ after calcination treatment or hydrothermal processing at high temperatures for a long period. The N doping level can be controlled by adjusting the calcination temperature and time [14]. A local $Ti^{3+}$ impurity is also generated by the calcination or hydrothermal process with reduction species (such as $H_2$ [20, 21], Al [22], and $NaBH_4$ [23]) and treatment with a high-energy particle flow, which contains N-ion implantation [24], UV-pulsed laser ablation [25], and spark plasma sintering [26]. However, considerably few studies have reported the codoping of N and $Ti^{3+}$. These studies are based on the fact that nonmetal doping produces O vacancies and $Ti^{3+}$, and reduction agents must be used in the procedure if it works; this method also requires an uncontrollable doping concentration and a large amount of time. In general, all of these doping routes (such as N and $Ti^{3+}$) exhibit low efficiency, high-power dissipation, and considerable time consumption; these routes involve N species or reduction species in a high-temperature environment with external energy imported to keep N or reduction species active. In particular, a two-step process is required for the reduction species ($H_2$) and N source ($NH_3$); long annealing treatment is also needed to obtain N- and $Ti^{3+}$-codoped $TiO_2$ (NT–$TiO_2$) with tunable doping levels [13]. In this regard, determining an ultrafast one-step approach and new reduction species is a mainstream, but it remains a challenge for efficient doping.

An energetic material (EM) is a reactive substance that contains a large amount of potential energy [27]. This substance can be initiated to undergo substantially rapid, self-propagating reactions, generate various radicals and gas products during the reconstruction of chemical bonds, and liberate heat. In the present work, an ultrafast, one-step $NaN_3$ deflagration route is rationally designed for synthesizing NT–$TiO_2$. With regard to substances, the $NaN_3$ deflagration generates highly reactive species (N radicals and Na clusters) to provide both the N source and reduction species for the doping of N and $Ti^{3+}$ in a one-step process. With regard to energy, the deflagration produces an instantaneous high-temperature/pressure environment, improving the reactivity of N radicals and Na clusters for the realization of ultrafast doping. The resulting N and $Ti^{3+}$ codoping introduces impurity energy bands in NT–$TiO_2$, which can efficiently narrow the bandgap of $TiO_2$ and enhance its visible-light absorption. The EM deflagration approach provides a promising route for the ultrafast synthesis of other functional materials.

## 2 Experimental section

### 2.1 Synthesis of NT–$TiO_2$ microporous nanosheets

$TiO_2$ nanosheets were fabricated via a facile hydrothermal method. In a typical process, 3 mL of hydrofluoric acid was added dropwise into a 100-mL Teflon pot containing 25 mL of $Ti(OBu)_4$ while stirring. After 15 min of stirring at room temperature, the Teflon pot was sealed and kept at 200 °C for 24 h. Finally, after the resulting precipitate was centrifuged three times, washed with ethanol to remove the hydrofluoric acid and organics, and dried in a vacuum oven for 12 h, the as-prepared $TiO_2$ nanosheets were obtained.

Afterwards, 1.0 g of $TiO_2$ nanosheets and a certain amount of sodium azide ($NaN_3$) were added to 5 mL of deionized water while stirring under ultrasonic conditions for 30 min to obtain a white homogeneous suspension. The suspension was gradually poured into a crucible filled with liquid N and subsequently freeze-dried to obtain a mixture of $TiO_2$ and $NaN_3$. After the deflagration of $NaN_3$ in the mixture annealed to 450 °C in an $N_2$ atmosphere, the product was washed with deionized water more than three times and dried at 60 °C for 12 h in a vacuum oven. The product was labelled as NT–$TiO_2$–*X*, where *X* represents the amount of added $NaN_3$ (*X* × 100 mg).

### 2.2 Characterization

The $NaN_3/TiO_2$ mixture was examined via simultaneous thermogravimetric analysis (TGA) and differential scanning calorimetry (DSC; TGA-DSC 1/1100 LF, Mettler Toledo). The thermal analysis unit was coupled with a mass spectrometer for the intermediate radical species. The emission spectra were obtained using a Q-switched Nd:YAG laser at a wavelength of 532 nm and an energy density of 92 J/$cm^2$. The crystal structures of all the samples were examined via X-ray diffraction analysis (XRD, Bruker D8 Advance with Cu-K$\alpha$ radiation, $\lambda$ = 1.5418 Å). The morphology and particle size were determined via transmission electron microscopy (TEM, JEOL JSM-2010) with an accelerating voltage of 200 kV. UV–visible (vis) absorption spectra were obtained using a UV–vis spectrometer (Shimadzu UV-3600). The Raman spectra of the samples were recorded using a Renishaw Raman RE01 scope with a 785-nm infrared laser. Electron paramagnetic resonance (EPR) spectra were recorded at 110 K using a Bruker EMX-10/12 EPR spectrometer. X-ray photoelectron spectroscopy (XPS) was performed using an ESCALAB 250 XPS X-ray Electron Spectrometer (American Thermo Electron Corporation). The Brunauer–Emmett–Teller (BET) surface area and porosity of the samples were determined using a Micromeritics ASAP 2020 N adsorption apparatus.

### 2.3 Photoelectrochemical measurements

To measure the transient photocurrent responses, the as-prepared samples were fabricated as film electrodes via the following method: 5 mg of photocatalyst was added to 3 mL of absolute ethyl alcohol, and the mixture was ultrasonicated for 30 min to produce a homogeneous suspension. Subsequently, the suspension was coated dropwise onto F-doped $SnO_2$-coated glass (FTO glass) via the spin-coating method. Afterwards, the electrodes were calcined at 300 °C for 20 min. The photocurrents were measured using a quartz cell with a standard three-electrode system: The resultant electrode served as the working electrode, with an active area of approximately 1 $cm^2$, and the Pt plate and Ag/AgCl (saturating KCl) served as the counter and reference electrodes, respectively. A 300-W Xe arc lamp equipped with a UV cutoff filter ($\lambda$ > 400 nm) was utilized as the visible-light source. The electrolyte was a $Na_2SO_4$ (1 M) aqueous solution.

## 3 Results and discussion

### 3.1 Preparation of NT–$TiO_2$ nanosheets

Scheme 1 shows the entire procedure for the preparation of NT–$TiO_2$ by using $NaN_3$ and pristine $TiO_2$. First, a certain amount of as-prepared $TiO_2$ nanosheets and $NaN_3$ were added to deionized water to form a well-dispersed $TiO_2$ nanosheet suspension in $NaN_3$ solution via stirring and ultrasonic treatment. The suspension was poured into liquid N for quick freezing and subsequently freeze-dried. The quick freezing and freeze-drying are crucial for the sufficiently uniform mixing of $TiO_2$ and $NaN_3$. The mixture was placed in a tube furnace with $N_2$ flowing at 450 °C to trigger the $NaN_3$ deflagration. The tube furnace was used to observe the deflagration process and collect the product. N and $Ti^{3+}$ doping can occur and be completed after rapid deflagration in less than 1 s (Fig. 1 and Videos ESM1 and ESM2). The high-speed photographs of the deflagration process in Fig. S1 in the Electronic Supplementary Material (ESM) and the corresponding Video ESM3 show that the deflagration process was rapid: It can be completed in approximately 300 ms. This duration was considerably faster than those of other N or $Ti^{3+}$ doping techniques. These widely used techniques also involve time-consuming thermal annealing or hydrothermal procedures. After $NaN_3$ deflagration, the final products exhibited different but uniform colors with various amounts of $NaN_3$ (as shown Scheme 1), which indicates the successful one-step doping process.

### 3.2 Characterizations of NT–$TiO_2$ microporous nanosheets

To confirm the effects of $NaN_3$ deflagration on the

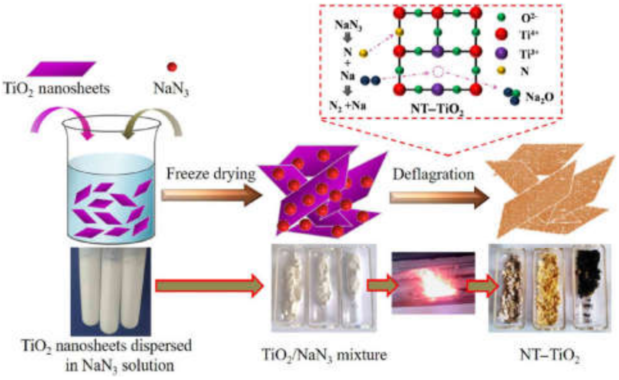

**Scheme 1** Schematic illustration of the formation of NT–$TiO_2$ nanosheets.

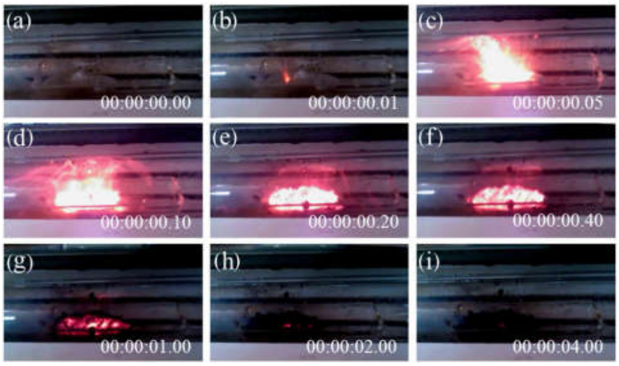

**Figure 1** Photos of the $NaN_3/TiO_2$ mixture deflagration process. A stepwise reaction started: (b) a minor initial ignition at 0.01 s, (d) followed by a major deflagration at 0.10 s, (f) termination at 0.40 s, and (i) cooling to the enviromental temperature at 4.0 s.

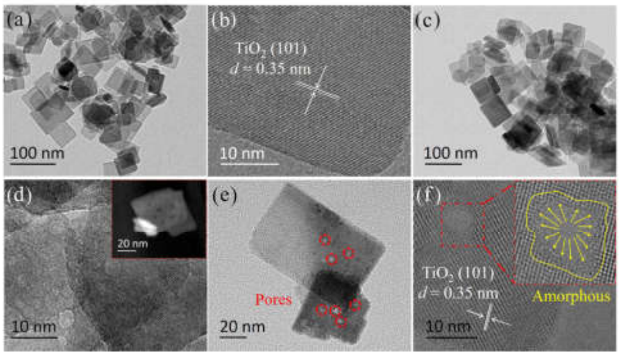

**Figure 2** TEM images of pristine $TiO_2$ (a) and (b) and NT–$TiO_2$–2 samples (c)–(f). Scale bars are shown in each image.

morphology of the obtained NT–$TiO_2$, the samples were characterized via TEM. The pristine $TiO_2$ obtained via the hydrothermal method exhibited square-shaped sheets with an average edge length of approximately 50 nm (Fig. 2(a)). Each $TiO_2$ nanosheet was a single crystal with a clean, smooth surface and an exposed (101) facet (0.35 nm in lattice plane spacing) (Fig. 2(b)). The NT–$TiO_2$–2 sample showed fragments with decreased sizes (Figs. 2(c)–2(f)). Unlike pristine $TiO_2$, the NT–$TiO_2$ sample surface became considerably rough, with the formation of numerous nanopits (Fig. 2(d)) and in-plane holes (Fig. 2(e) and Fig. S2 in the ESM). This texture is attributed to the etching effects of N radicals and Na clusters. The TEM images of NT–$TiO_2$–1 and NT–$TiO_2$–3 samples (Fig. S3 in the ESM) illustrate that many fragments with decreased sizes and pores were formed with an increased amount of added $NaN_3$. However, with excess $NaN_3$ addition, large $Na_{0.23}TiO_2$ particles were generated, as shown in Fig. S4 in the ESM. In the high-resolution TEM (HRTEM) image of Fig. 2(f), the $TiO_2$ section around the pores exhibits an amorphous morphology, and the remaining parts of the whole $TiO_2$ nanosheet maintain a single-crystal nanostructure with the (101) facet exposed. The amorphous morphology may result from the lattice distortion caused by the high concentration of N and $Ti^{3+}$ doping and O vacancies. The electron energy loss spectroscopy elemental mappings (Fig. S5 in the ESM) reveal that N, O, and Ti were homogeneously distributed within the NT–$TiO_2$–2 nanostructure, indicating the relatively uniform doping via the $NaN_3$ deflagration method.

To confirm the effects of $NaN_3$ deflagration on the doping and structural changes in the obtained NT–$TiO_2$, XRD, Raman spectroscopy, electron paramagnetic resonance spectroscopy, and XPS were performed.

The XRD patterns of pristine $TiO_2$ nanosheets and NT–$TiO_2$ microporous nanosheets are shown in Fig. 3(a). The diffraction peaks in the XRD pattern of the pure $TiO_2$ sample marked in black at 25.3°, 37.8°, 48.0°, 55.0°, 62.6°, 70.3°, and 75.0° were indexed to the (101), (004), (200), (211), (204), (220), and (215) planes of $TiO_2$ (JCPDS Card 21-1272), respectively. The XRD patterns of the NT–$TiO_2$ samples obtained with different amounts of $NaN_3$ deflagration treatment are identical to those of pristine $TiO_2$ nanosheets. Figure 3(b) shows the Raman spectra of pure $TiO_2$ nanosheets and NT–$TiO_2$ microporous nanosheets. Four Raman peaks at 149, 409, 515, and 633 $cm^{-1}$ can be observed for the pure $TiO_2$ sample, which correspond to the $E_g$, $B_{1g}$, $A_{1g}$, and $E_g$ modes of the anatase-phase $TiO_2$,

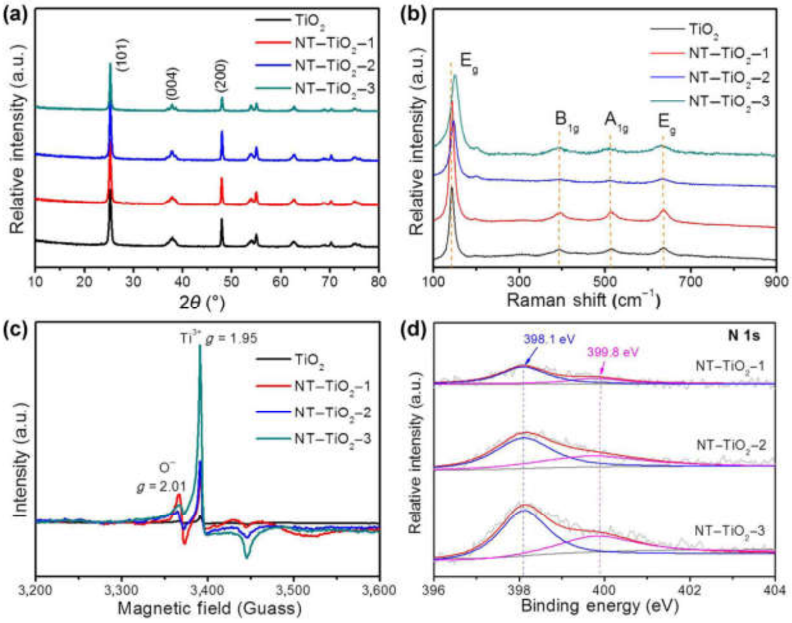

**Figure 3** Characterization of the obtained NT–$TiO_2$ microporous nanosheets. (a) X-ray diffraction curves, (b) Raman spectra of pristine $TiO_2$ and NT–$TiO_2$ samples, (c) electron paramagnetic resonance spectra, and (d) N 1s XPS spectra of NT–$TiO_2$ samples.

respectively. After $NaN_3$ deflagration, nearly all the NT–$TiO_2$ microporous nanosheet samples showed the same Raman peaks, indicating that they had the same crystal structure. Nevertheless, the $E_g$ mode of NT–$TiO_2$–3 sample shifted from 149 to 165 $cm^{-1}$, which suggests the change in the Ti–O bond with excess $NaN_3$ addition. Notably, the $TiO_2$ rutile phase showed no Raman peaks. The XRD patterns and Raman spectra of the NT–$TiO_2$ samples showed no significant change compared with those of pristine $TiO_2$. This indicates that the obtained NT–$TiO_2$ samples retained their crystal structure and the phase of pristine $TiO_2$. However, excess $NaN_3$ addition can lead to the formation of impurities ($Na_{0.23}TiO_2$, Fig. S6 in the ESM). Thus, the addition of $NaN_3$ must be controlled.

The presence of $Ti^{3+}$ in the NT–$TiO_2$ samples was supported by the EPR spectroscopy results. As shown in Fig. 3(c), two strong EPR signals were observed at $g$ = 1.95 and 2.01 compared with pristine $TiO_2$; these signals can be assigned to $Ti^{3+}$ and O vacancies ($O^-$), respectively. In addition, the intensity of the EPR peaks of $Ti^{3+}$ and $O^-$ increased with the amount of $NaN_3$. The doping conditions and chemical compositions of the NT–$TiO_2$ samples were investigated via XPS. The XPS peaks of N 1s at 399.8 and 398.1 eV of the NT–$TiO_2$ samples were assigned to the N atoms located at the interstitial sites of the $TiO_2$ lattice [17] and substitutional N in the N–Ti–O structure [28], respectively (Fig. 3(d)). Similar to other dry-process methods, substitutional N was dominant, with a percentage of ~ 75%, according to the area ratio of N 1s peaks. The N doping (atomic percentage of N in the measured C, O, Ti, and N elements from XPS) concentration increased with the $NaN_3$ amount; the concentrations were 1.46 at.%, 2.65 at.%, and 3.48 at.% for samples NT–$TiO_2$–1, NT–$TiO_2$–2, and NT–$TiO_2$–3, respectively (Table S1 in the ESM). The XPS features of Ti 2p were observed at 458.7 and 464.5 eV for $TiO_2$, which can be assigned to $Ti^{4+}$. With increased $NaN_3$, both Ti 2p3/2 and Ti 2p1/2 XPS peaks broadened and shifted towards a low binding energy, which suggests different chemical bonding environments with $Ti^{3+}$ doping (Fig. S7(a) in the ESM). XPS data analysis demonstrated that the $NaN_3$ treatment achieved N doping and reduced the partial $Ti^{4+}$ in $TiO_2$ to $Ti^{3+}$. Additionally, according to the complete XPS spectra (Fig. S7(b) in the ESM), no other elements, except C, N, Ti, and O, can be detected, reveals the advantages of our designed $NaN_3$ deflagration method with regard to purity.

### 3.3 Light absorption and photoelectrochemical properties of NT–$TiO_2$ samples

Figure 4(a) shows the UV–vis absorption spectra of pristine $TiO_2$ and NT–$TiO_2$ samples. The absorption edge of the pristine $TiO_2$ nanosheets was approximately 387 nm, which corresponds to a bandgap of approximately 3.2 eV according to the formula $\lambda = 1239.8/E_g$. Nonetheless, a secondary absorption edge at approximately 520 nm was observed in the NT–$TiO_2$ samples, which is attributed to the additional valence states from doped N atoms [29]. The bandgap at 2.38 eV is consistent with the Tauc plot for bandgap determination results (Fig. S8 in the ESM). In addition to the absorption edge shifting, the light absorption intensity in the visible region of the NT–$TiO_2$ samples was considerably higher than that of pristine $TiO_2$. Notably, with the increased amount of $NaN_3$, the NT–$TiO_2$ samples exhibited an upward trend from 550 to 800 nm in the visible-light region, which is attributed to the existence of $Ti^{3+}$ [22]. In general, the variation in the absorption spectrum consisted of two main parts: One part is attributed to the generation of the new absorption edge at 520 nm due to N doping, and the other part is attributed to the $Ti^{3+}$ doping that caused visible-light absorption in the long-wavelength region. Therefore, the light-absorption differences in the NT–$TiO_2$ samples are attributed to the band engineering caused by the codoping of N and $Ti^{3+}$ with different concentrations. Consequently, their sample colors changed from gray or yellow to green (inset in Fig. 4(a)) or blue and black (Fig. S9 in the ESM).

The transient photocurrents of the NT–$TiO_2$ samples were measured to show their visible-light responses. For all the NT–$TiO_2$ samples, the increase and decrease in the photocurrents responded rapidly to the light irradiation being switched on and off (Fig. 4(b)). The photocurrent density of pristine $TiO_2$ under visible-light irradiation was approximately 0.4 μA/cm$^2$, and those of NT–$TiO_2$–1, NT–$TiO_2$–2, and NT–$TiO_2$–3 were approximately 0.5, 2.0, and 1.4 μA/cm$^2$, respectively. This density was highly enhanced after codoping of N and $Ti^{3+}$ via $NaN_3$ deflagration treatment.

NT–$TiO_2$–2 showed the highest photocurrent under visible-light irradiation, which is attributed to the moderate doping level of N and $Ti^{3+}$. In other words, N doping introduces a higher valence band ($N_{2p}$), and $Ti^{3+}$ doping can form an intermediate energy level below the conduction band in NT-$TiO_2$, which narrow the bandgap of $TiO_2$ and improve the visible-light response of NT-$TiO_2$. However, excess N and $Ti^{3+}$ doping generally produces combination centers for electrons and holes, reduces the concentration of photogenerated carriers, and reduces the photocurrent. Additionally, the appropriate amount of added $NaN_3$ makes NT–$TiO_2$–2 possess the largest BET specific surface area, which is beneficial for the improvement of its photoresponse.

### 3.4 Mechanisms of ultrafast doping process

To obtain further information about the ultrafast doping process, the $NaN_3$ deflagration features and subsequent doping mechanisms in the mixture were investigated via a series of characterization techniques. The mass spectrum was determined to confirm the generation of N radicals, as shown in Fig. 5(a). The main deflagration products of $NaN_3$ were $N_2$ and N radicals with *m*/*e* at 28 and 14. The signals at *m*/*e* at 17 and 18 are attributed to ionized $OH^-$ and $H_2O^-$ species

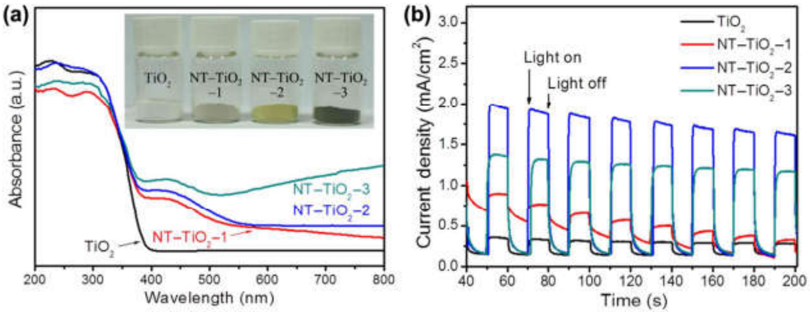

**Figure 4** (a) Diffuse reflectance UV–vis spectra. Inset: optical image for pristine $TiO_2$ and NT–$TiO_2$ samples. (b) Transient photocurrent responses of $TiO_2$ and NT–$TiO_2$ samples under visible-light irradiation.

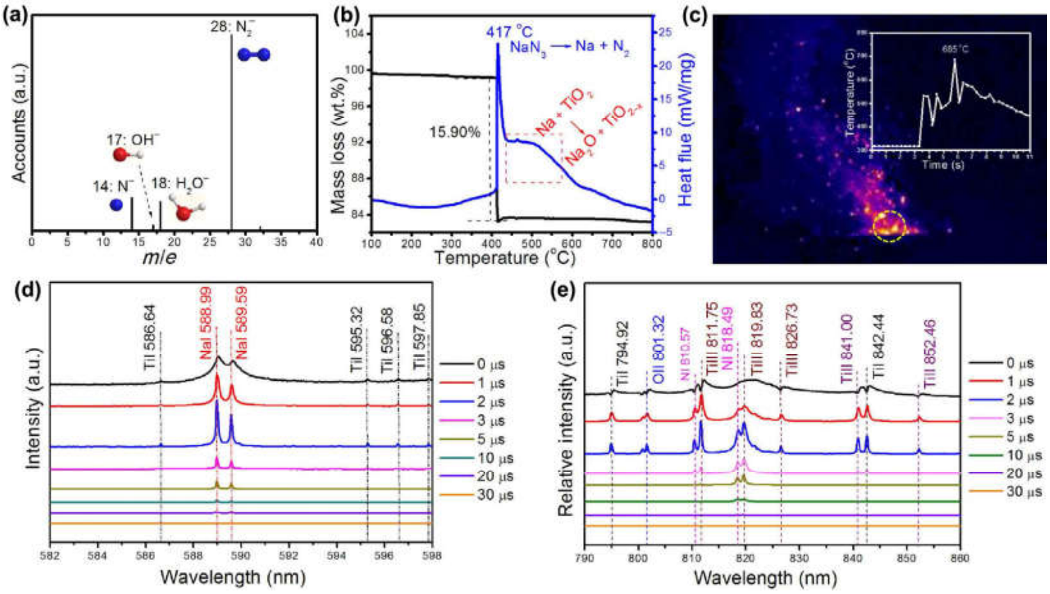

**Figure 5** (a) Mass spectra and (b) TGA/DSC curves of the $TiO_2$ nanosheets and $NaN_3$ mixture. (c) IR image of the $TiO_2/NaN_3$ mixture deflagration process. Inset: measured temperature in the marked area. (d) and (e) Delayed time-dependent emission spectra of $TiO_2$ and $NaN_3$ mixture generated with a 532-nm laser at 90 J/cm$^2$.

from the absorbed $H_2O$ in the $NaN_3$ and $TiO_2$ mixture. The TGA/DSC curves in Fig. 5(b) show that $NaN_3$ exploded at 417 °C and lost 15.9 wt.% of the whole $NaN_3/TiO_2$ mixture with the release of $N_2$. In addition to the main heat flux peak at 417 °C, a broad peak due to the heat released from the subsequent redox reaction between Na and $TiO_2$ was observed.

To elucidate the temperature-field variation due to heat liberation in the deflagration process, infrared (IR) temperature measurement was conducted. As shown in Fig. 5(c), many fire sparks were distributed uniformly in the furnace, indicating a homogeneous reaction environment. The time-dependent temperature curve in the marked area reveals that the deflagration temperature was high at 685 °C and was maintained for only a few seconds. Notably, a high temperature can increase the reactivity of N radicals and Na clusters and promote the N and $Ti^{3+}$ doping process. Moreover, a short duration of a high temperature protected $TiO_2$ against phase transformation from anatase to rutile.

The intermediates in the deflagration process of the $NaN_3/TiO_2$ mixture were identified using the time-resolved emission spectra (Figs. 5(d) and 5(e)). Two main emission peaks at 588.99 and 589.59 nm are attributed to the Na generated by $NaN_3$ deflagration (Fig. 5(d)). Several Ti I emission peaks were observed, revealing the formation of Ti metal from the O atoms captured by Na in the $TiO_2$ crystal (Fig. 5(d)). Additionally, Ti species with other valence states (Ti II and Ti III), as well as N radicals (N I) and O I, were detected (Fig. 5(e)). This observation confirmed the formation of N radicals and reactions between Na and $TiO_2$. On the basis of the delayed time-dependent intensity distribution of emission peaks, we inferred that the doping process was completed at microseconds because the N radicals and other Ti or O species increased in the first few microseconds and disappeared in less than 30 μs. Therefore, the high reactivity of N radicals and Na clusters and high deflagration temperature should be responsible for the successful ultrafast doping.

## 4 Conclusions

The present study provides an ultrafast and effective approach for fabricating NT–$TiO_2$ microporous nanosheets. The doping process can be completed in 1 s. The NT–$TiO_2$ samples showed rough surfaces with nanopits and nanopores due to N radicals and Na cluster etching effects. The doping concentrations of N and $Ti^{3+}$ can be easily controlled by adjusting the $NaN_3$ addition. NT–$TiO_2$ samples showed significant enhancements in the visible-light absorption and photoelectric response. Furthermore, this EM deflagration synthesis technique can be utilized for the ultrafast fabrication of other multielement codoped semiconductor photocatalysts with tunable bandgaps.

## Acknowledgements

This work was supported by the National Natural Science Foundation of China (Nos. 11272292, 11372288, 11502242, 51402269 and 11502247), Development Foundation of CAEP (No. 2014B0302041), the Applied Basic Research Program of Sichuan Province (No. 2015JY0229), the Open Project of State Key Laboratory Cultivation Base for Nonmetal Composites and Functional Materials (No. 14zxfk08) and China Postdoctoral Science Foundation (No. 2016M592702).

**Electronic Supplementary Material**: Supplementary material (detailed information that includes high-speed photographs of the deflagration process; pore size distribution spectra and $N_2$ adsorption/desorption isotherms of $TiO_2$ and NT–$TiO_2$ samples; TEM images of the NT–$TiO_2$–1, NT–$TiO_2$–3, and NT–$TiO_2$–10 samples; STEM images and N, O, and Ti elemental mappings of the NT–$TiO_2$–2 sample; XRD patterns of NT–$TiO_2$–6 and NT–$TiO_2$–10 samples; atomic ratios of Ti, O, N, and C in the obtained NT–$TiO_2$ samples; Ti 2p and full XPS spectra of pristine $TiO_2$ and NT–$TiO_2$ samples; Tauc plot for band gap determination from the diffuse reflectance ultraviolet–visible spectra; diffused reflectance ultraviolet–visible spectra of $TiO_2$, NT–$TiO_2$–2, NT–$TiO_2$–10, and M–$TiO_2$–2 samples and their optical image; and deflagration process videos) is available in the online version of this article at https://doi.org/10.1007/s12274-018-2058-0.

## References

[1] Chen, X. B.; Mao, S. S. Titanium dioxide nanomaterials: Synthesis, properties, modifications, and applications. *Chem. Rev.* **2007**, *107*, 2891–2959.

[2] Feng, X. J.; Zhu, K.; Frank, A. J.; Grimes, C. A.; Mallouk, T. E. Rapid charge transport in dye-sensitized solar cells made from vertically aligned single-crystal rutile $TiO_2$ nanowires. *Angew. Chem., Int. Ed.* **2012**, *51*, 2727–2730.

[3] Chen, X. B.; Shen, S. H.; Guo, L. J.; Mao, S. S. Semiconductor-based photocatalytic hydrogen generation. *Chem. Rev.* **2010**, *110*, 6503–6570.

[4] Subbiah, G.; Premanathan, M.; Kim, S. J.; Krishnamoorthy, K.; Jeyasubramanian, K. Preparation of $TiO_2$ nanopaint using ball milling process and investigation on its antibacterial properties. *Mater. Express* **2014**, *4*, 393–399.

[5] Moon, H. G.; Shim, Y. S.; Jang, H. W.; Kim, J. S.; Choi, K. J.; Kang, C. Y.; Choi, J. W.; Park, H. H.; Yoon, S. J. Highly sensitive CO sensors based on cross-linked $TiO_2$ hollow hemispheres. Sensor. *Actuat. B-Chem.* **2010**, *149*, 116–121.

[6] Hu, H.; Yu, L.; Gao, X. H.; Lin, Z.; Lou, X. W. Hierarchical tubular structures constructed from ultrathin $TiO_2$(B) nanosheets for highly reversible lithium storage. *Energ. Environ. Sci.* **2015**, *8*, 1480–1483.

[7] Guan, B. Y.; Yu, L.; Li, J.; Lou, X. W. A universal cooperative assembly-directed method for coating of mesoporous $TiO_2$ nanoshells with enhanced lithium storage properties. *Sci. Adv.* **2016**, *2*, e1501554.

[8] Hoffmann, M. R.; Martin, S. T.; Choi, W.; Bahnemann, D. W. Environmental applications of semiconductor photocatalysis. *Chem. Rev.* **1995**, *95*, 69–96.

[9] Chen, X. B.; Liu, L.; Yu, P. Y.; Mao, S. S. Increasing solar absorption for photocatalysis with black hydrogenated titanium dioxide nanocrystals. *Science* **2011**, *331*, 746–750.

[10] Lin, T. Q.; Yang, C. Y.; Wang, Z.; Yin, H.; Lü, X. J.; Huang, F. Q.; Lin, J. H.; Xie, X. M.; Jiang, M. H. Effective nonmetal incorporation in black titania with enhanced solar energy utilization. *Energy Environ. Sci.* **2014**, *7*, 967–972.

[11] Sinhamahapatra, A.; Jeon, J. P.; Yu, J. S. A new approach to prepare highly active and stable black titania for visible light-assisted hydrogen production. *Energy Environ. Sci.* **2015**, *8*, 3539–3544.

[12] Liu, N.; Schneider, C.; Freitag, D.; Hartmann, M.; Venkatesan, U.; Muller, J.; Spiecker, E.; Schmuki, P. Black $TiO_2$ nanotubes: Cocatalyst-free open-circuit hydrogen generation. *Nano Lett.* **2014**, *14*, 3309–3313.

[13] Hoang, S.; Berglund, S. P.; Hahn, N. T.; Bard, A. J.; Mullins, C. B. Enhancing visible light photo-oxidation of water with $TiO_2$ nanowire arrays via cotreatment with $H_2$ and $NH_3$: Synergistic effects between $Ti^{3+}$ and N. *J. Am. Chem. Soc.* **2012**, *134*, 3659–3662.

[14] Irie, H.; Watanabe, Y.; Hashimoto, K. Nitrogen-concentration dependence on photocatalytic activity of $TiO_{2-x}N_x$ powders. *J. Phys. Chem. B* **2003**, *107*, 5483–5486.

[15] Wang, J.; Tafen, D. N.; Lewis, J. P.; Hong, Z. L.; Manivannan, A.; Zhi, M. J.; Li, M.; Wu, N. Q. Origin of photocatalytic activity of nitrogen-doped $TiO_2$ nanobelts. *J. Am. Chem. Soc.* **2009**, *131*, 12290–12297.

[16] Jiang, Z.; Yang, F.; Luo, N. J.; Chu, B. T. T.; Sun, D. Y.; Shi, H. H.; Xiao, T. C.; Edwards, P. P. Solvothermal synthesis of N-doped $TiO_2$ nanotubes for visible-light-responsive photocatalysis. *Chem. Commun.* **2008**, 6372–6374.

[17] Livraghi, S.; Paganini, M. C.; Giamello, E.; Selloni, A.; Di Valentin, C.; Pacchioni, G. Origin of photoactivity of nitrogen-doped titanium dioxide under visible light. *J. Am. Chem. Soc.* **2006**, *128*, 15666–15671.

[18] Antony, R. P.; Mathews, T.; Panda, K.; Sundaravel, B.; Dash, S.; Tyagi, A. K. Enhanced field emission properties of electrochemically synthesized self-aligned nitrogen-doped $TiO_2$ nanotube array thin films. *J. Phys. Chem. C* **2012**, *116*, 16740–16746.

[19] Shi, N.; Li, X. H.; Fan, T. X.; Zhou, H.; Ding, J.; Zhang, D.; Zhu, H. X. Biogenic N-I-codoped $TiO_2$ photocatalyst derived from kelp for efficient dye degradation. *Energy Environ. Sci.* **2011**, *4*, 172–180.

[20] Zheng, Z. K.; Huang, B. B.; Meng, X. D.; Wang, J. P.; Wang, S. Y.; Lou, Z. Z.; Wang, Z. Y.; Qin, X. Y.; Zhang, X. Y.; Dai, Y. Metallic zinc-assisted synthesis of $Ti^{3+}$ self-doped $TiO_2$ with tunable phase composition and visible-light photocatalytic activity. *Chem. Commun.* **2013**, *49*, 868–870.

[21] Zuo, F.; Bozhilov, K.; Dillon, R. J.; Wang, L.; Smith, P.; Zhao, X.; Bardeen, C.; Feng, P. Y. Active facets on titanium(III)-doped $TiO_2$: An effective strategy to improve the visible-light photocatalytic activity. *Angew. Chem., Int. Ed.* **2012**, *124*, 6327–6330.

[22] Wang, Z.; Yang, C. Y.; Lin, T. Q.; Yin, H.; Chen, P.; Wan, D. Y.; Xu, F. F.; Huang, F. Q.; Lin, J. H.; Xie, X. M. et al. Visible-light photocatalytic, solar thermal and photoelectrochemical properties of aluminium-reduced black titania. *Energy Environ. Sci.* **2013**, *6*, 3007–3014.

[23] Fang, W. Z.; Xing, M. Y.; Zhang, J. L. A new approach to prepare $Ti^{3+}$ self-doped $TiO_2$ via $NaBH_4$ reduction and hydrochloric acid treatment. *Appl. Catal. B: Environ.* **2014**, *160–161*, 240–246.

[24] Zhou, X. M.; Häublein, V.; Liu, N.; Nguyen, N. T.; Zolnhofer, E. M.; Tsuchiya, H.; Killian, M. S.; Meyer, K.; Frey, L.; Schmuki, P. $TiO_2$ nanotubes: Nitrogen-ion implantation at low dose provides noble-metal-free photocatalytic $H_2$-evolution activity. *Angew. Chem., Int. Ed.* **2016**, *55*, 3763–3767.

[25] Pan, S. S.; Liu, X. L.; Guo, M.; Yu, S. F.; Huang, H. T.; Fan, H. T.; Li, G. H. Engineering the intermediate band states in amorphous $Ti^{3+}$-doped $TiO_2$ for hybrid dye-sensitized solar cell applications. *J. Mater. Chem. A* **2015**, *3*, 11437–11443.

[26] Yang, Y. C.; Zhang, T.; Le, L.; Ruan, X. F.; Fang, P. F.; Pan, C. X.; Xiong, R.; Shi, J.; Wei, J. H. Quick and facile preparation of visible light-driven $TiO_2$ photocatalyst with high absorption and photocatalytic activity. *Sci. Rep.* **2014**, *4*, 7045.

[27] Badgujar, D. M.; Talawar, M. B.; Asthana, S. N.; Mahulikar, P. P. Advances in science and technology of modern energetic materials: An overview. *J. Hazard. Mater.* **2008**, *151*, 289–305.

[28] Sathish, M.; Viswanathan, B.; Viswanath, R. P.; Gopinath, C. S. Synthesis, characterization, electronic structure, and photocatalytic activity of nitrogen-doped $TiO_2$ nanocatalyst. *Chem. Mater.* **2005**, *17*, 6349–6353.

[29] Liu, G.; Yin, L. C.; Wang, J. Q.; Niu, P.; Zhen, C.; Xie, Y. P.; Cheng, H. M. A red anatase $TiO_2$ photocatalyst for solar energy conversion. *Energy Environ. Sci.* **2012**, *5*, 9603–9610.